Rapid Updating and Improvement of Airborne LIDAR DEMs Through Ground-Based SfM 3-D Modeling of Volcanic Features

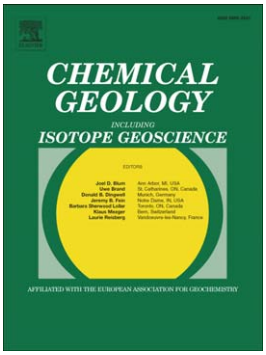

Modelling configurational entropy of silicate melts

¡!–[INS][J. K.]–¿J.K.¡!–[/INS]–¿ Russell, D. Giordano

PII: S0009-2541(16)30361-8
DOI: doi: 10.1016/j.chemgeo.2016.07.019
Reference: CHEMGE 18007

To appear in: *Chemical Geology*

Received date: 6 March 2016
Revised date: 13 June 2016
Accepted date: 22 July 2016

Please cite this article as: Russell, ¡.!.–[.I.N.S.].[.J.K.].–¿.J.K.¡.!.–[./.I.N.S.].–¿., Giordano, D., Modelling configurational entropy of silicate melts, *Chemical Geology* (2016), doi: 10.1016/j.chemgeo.2016.07.019

Modelling Configurational Entropy of Silicate Melts

J. K. Russell
Department of Earth, Ocean and Atmospheric Sciences
The University of British Columbia
Vancouver, B.C., V6T 1Z4

D. Giordano
Earth Sciences department, University of Torino
Via Valperga Caluso, 35,
10125 Torino, Italy

Chemical Geology
(Silicate Melts Special Issue)

Submitted March 6, 2016
Revised June 11, 2016

Corresponding Author:
Kelly Russell krussell@eos.ubc.ca

Abstract

The Adam-Gibbs theory provides a robust connection between the transport or relaxation properties of melts and their thermochemical properties. In its expanded form:

$$log\,\eta = A + \frac{B}{T\,[S_c(Tg) + Cp_c\,ln\,(T/Tg)}$$

the equation has adjustable unknown parameters *A*, *B* and $S_c(Tg)$ which can be estimated from experimental estimates of configurational heat capacity (Cp_c), glass transition temperature (*Tg*) and viscosity (η). Here, we use recently published datasets for anhydrous and hydrous silicate melts and glasses (N~50) for which there are measurements of *log* η and calorimetric measurements of Cp_c and *Tg*. Our fitting strategy follows the approach developed by previous workers with the sole exception that we assume all silicate melts converge to a common, but unknown, high temperature limit to melt viscosity (e.g., *A* = log η_∞). Our optimal value for *A* is -3.51 ±0.25. A consequence of a common, high-temperature limit to silicate melt viscosity is that the corresponding model values of glass transition temperature (Tg^{12}), melt fragility (*m*), and the ratio Cp_c/S_c are constrained to lie on a single plane approximated as:

$$\frac{Cp_c}{S_c} = -\frac{Tg^{12}}{243399} - \frac{m}{15.518} + 0.996$$

thereby establishing a quantitative connection between calorimetric and rheological measurements. Lastly, we show a good correspondence between values of Tg^{12} and fragility (*m*) from this Adam-Gibbs based model of melt viscosity and values predicted by the GRD viscosity model for multicomponent silicate melts (cf. Giordano et al. 2008).

Introduction

Entropy is a thermochemical property of silicate melts and glasses that cannot be measured directly; rather it is computed or deduced. The entropy of silicate melts is also a direct reflection of the melt's structural properties (i.e. configuration) and, thus, has the capacity to connect thermochemistry and rheology via the structural configuration of silicate melts.

The Adam-Gibbs theory provides a robust connection between the transport properties, relaxation timescales of of melts, and their thermochemical properties (Adam and Gibbs, 1965; Richet, 1984; Richet and Bottinga, 1986;1995; Avramov, 2013; Jensen and Jakobsen 2015; Giordano et al. 2015). Following configurational entropy theory, the temperature dependence of melt viscosity (η) is described by:

$$log\,\eta = A + \frac{B}{T \cdot S_c(T)} \qquad (1)$$

where S_c is the configurational entropy of the melt at temperature (T), B is proportional to the activation energy required for structural rearrangements supporting viscous flow, and A is the limiting viscosity of the melt at high temperatures (Adam and Gibbs, 1965; Richet, 1984). The Adam-Gibbs (AG) equation offers a quasi-theoretical means of accommodating the non-Arrhenian temperature dependence of viscosity (Richet and Bottinga 1995; Angell 1991; Bottinga et al. 1995). It is also shown to be an effective descriptor of viscosity over the compositional range of most geochemically-relevant melts (e.g., strong to fragile melts; Angell, 1985; Richet 1984; Richet and Bottinga, 1995; Baker 1996; Whittington et al. 2009).

Experimentally derived values of heat capacity across the glass transition

temperature are critical in order to uniquely solve for the contributions of the parameters *B* and $S_c(T)$ (e.g., Toplis et al. 1997; Webb, 2008). To this end, the AG function (Eq. 1) can be expanded by introducing the concept of the glass transition temperature:

$$log\ \eta\ =\ A\ +\ \frac{B}{T\left[S_c(Tg)\ +\ \int_{Tg}^{T}\frac{Cp(T)}{T}\,dt\right]} \quad (2)$$

where $S_c(Tg)$ is the residual configurational entropy of the investigated sample at the glass transition temperature. The integral of $Cp(T)$ in equation 2 is the heat capacity of the melt taken over the temperature interval marking the glass transition from an unequivocally defined glass transition temperature (Tg) to a higher temperature (T) where the melt is fully relaxed (Richet, 1984; Bottinga and Richet, 1996). The usual simplification is that silicate melt heat capacity (Cp_{melt}) is independent of temperature allowing $Cp(T)$ to be replaced by a constant representing the change in configurational heat capacity (Cp_c) associated with the glass to melt transition (i.e. $Cp_c = Cp_{melt} - Cp_g$) yielding the expression:

$$log\ \eta\ =\ A\ +\ \frac{B}{T\left[S_c(Tg)\ +\ Cp_c\ ln(^{T}/_{Tg})\right]} \quad . \quad (3)$$

Richet (1984) and Richet and Bottinga (1986) illustrated how the magnitude of $S_c(Tg)$ could be recovered from the calorimetric cycle using enthalpy and heat capacity data available for crystalline material and for the glass and melt counterparts. Alternatively, equation 3 can be fit to mixed datasets comprising calorimetric estimates of Tg and Cp_c and measurements of melt viscosity to calculate values of *A*, *B* and $S_c(Tg)$ (e.g., Richet and Neuville, 1992; Richet and Bottinga, 1995; Giordano et al. 2015). This approach has been adopted and modified by several subsequent workers (e.g., Toplis, 1998; Webb, 2008; Whittington et al. 2009; Avramov, 2013). Here, we use this strategy to investigate the

linkages between transport properties and calorimetric properties for a suite of anhydrous and hydrous, multicomponent silicate melts for which, both, calorimetric and viscosity data are available.

The Data

Our analysis is based, largely, on published datasets for which there are experimentally measured values of melt viscosity and corresponding calorimetric measurements of *Tg* and Cp_c. The calorimetric measurements derive from differential scanning calorimetric (DSC) experiments on glasses and melts (Fig. A1; Supplementary Materials) and the methods are more fully described in Giordano et al. (2015). Our experimental database comprises high temperature measurements on anhydrous and hydrous, multicomponent silicate melts. For inclusion in the database (Table 1), the melts must have the following attributes, including: i) well characterised melt compositions, ii) measured volatile (i.e. H_2O) contents, iii) calorimetrically measured values for the onset of the glass transition (Tg_{onset}) and for the fully relaxed melt (Tg_{melt}), iv) values of Cp_c based on observations of the heat capacity across the glass transition, and v) three or more measured values of viscosity at temperatures above the glass transition temperature. The methods for estimating values of Tg_{onset}, Tg_{melt}, and Cp_c from DSC measurements are explained more fully in Figure A1 (Supplementary Materials).

The compiled database incorporates 14 nominally anhydrous, melt compositions and 36 hydrous melt compositions giving us a total of 50 different melt compositions for which we have compiled 452 viscosity measurements (Table 1). Our dataset, including data sources, is described in Table 1 (e.g., Bouhfid et al. 2006; 2013; Giordano et al. 2015; Di

Genova et al. 2014; Robert et al. 2014) and the full oxide chemical compositions are reported in Table A1 (Supplementary Materials).

Figure 1 shows the measured properties of silicate melts used in this study. The chemical compositions of the 50 experimental melts are represented as SiO_2 versus Na_2O + K_2O (wt. %). Anhydrous melts are shown as solid black symbols and hydrous melts as grey circles. In this figure (and subsequent figures), the sizes of grey symbols denoting hydrous melts are proportional to their reported water contents. The melt compositions range from alkaline (e.g., latite, tephrite, phonolite, pantellerite) to subalkaline (e.g., basaltic andesite, rhyolite) and also include synthetic haplogranite and several anorthite - diopside mixtures. Water contents range from 0 to 6.3 wt. % (Fig. 1A). Measured values of Tg_{onset} are plotted against the temperature of the fully relaxed melt (Tg_{melt}) and define a linear trend parallel to the 1:1 line and have an average offset of ~60 K (Fig. 1B). Measured values of Cp_c show a strong decrease with increasing SiO_2 content (Fig. 1C) indicative of a shift from *fragile* to *strong* melts (Angell, 1985, Angell et al. 2000) and suggesting a greater degree of polymerization and minor structural re-ordering across the glass transition. The effects of increasing dissolved H_2O content are not systematic enough to define a single pattern (Fig. 1C).

The 452 measurements of melt viscosity span a temperature range of 585 - 2450 K (Figure 2). Measured values of viscosity are from 10^{-1} to 10^{14} Pa s. These experiments commonly use an anhydrous melt as a base composition to which volatiles have been added. In general, the hydrous melts were synthesized at elevated pressure and temperature below their solubility limits and quenched isobarically to produce homogeneous unvesiculated hydrous glasses (e.g., Richet et al. 1996; Richet and Toplis, 2001; Di Genova

et al. 2014). The viscosity measurements for hydrous silicate melts are restricted to a narrower range of temperatures immediately above their respective glass transition temperatures to avoid syn-experiment vesiculation or crystallization.

Modelling Methodology

Below we fit the expanded form of the Adam-Gibbs function (Eq. 3) to the calorimetrically measured values of Cp_c and Tg_{onset} and to measurements of melt viscosity. We mainly follow the methods of Richet (1984), Richet and Bottinga (1986; 1995), Toplis et al. (1997), Toplis (1998), Richet and Neuville (1992), and Webb (2008). However, our optimization strategy follows the work of Russell et al. (2002; 2003) and Russell & Giordano (2005) which propose that all silicate melts converge to a single, common, value of viscosity at high temperature (i.e. T >> $T_{liquidus}$). The implication is that the parameter *A*, the high temperature limit to Eq. 3, is a single constant for all melts in the dataset. This approach provides a more robust means of estimating $S_c(Tg)$ from fitting of the Adam-Gibbs function to viscosity data because: i) it reduces the number of unknown parameters, ii) it results in more meaningful correlations between the other parameters (e.g., Russell et al. 2002), and iii) it consigns the effects of melt composition and water content to only two parameters *B* and $S_c(Tg)$. Full details are provided in Giordano et al. (2015; see Appendix).

The main attributes of this optimization strategy are illustrated using a subset of 4 compositions, comprising anhydrous and hydrous equivalents of a phonolite (Phon, $Phon_{0.5}$) and a trachybasalt (Etn $Etn_{1.64}$). This subset of data is chosen because the 4 melts have variable numbers of viscosity measurements (N= 6 to 20) and spanning different ranges of temperature. The anhydrous melts feature low and high temperature

measurements whilst the hydrous melts have only low temperature data.

The dataset for each melt composition can be organized as a system of non-linear equations of the form:

$$log\ \eta_i = A + \frac{B}{T_i\ [S_c(Tg) + Cp_c\ ln(^{T_i}/_{Tg})\ ]} \qquad for\ i = 1{:}n \qquad (4)$$

where the three adjustable parameters *A, B,* $S_c(Tg)$ are unique unknowns for each melt composition and *n* is the number of measured pairs of log η:*T*(K). Equation 4 is non-linear in its parameters and is solved, here, by conventional iterative methods using a χ^2 merit function weighted to the experimental uncertainties on melt viscosity (e.g., Press et al. 1986; Russell et al. 2002). Specifically, we solved the system of equations using the Newton-Raphson method and we used explicit differentials of Eq. 4 to populate and update the (n x 3) Jacobian matrix for each iteration. Our optimal solution is checked two ways to ensure that we have found the global and local minimum. Firstly, we solve the system of equations using 3 significantly different initial guesses for *A*, *B*, and $S_c(Tg)$ guess (all having positive numbers). In each cases we recovered identical solutions within < 200 iterations. Secondly, we contoured the residuals on the solution surface surrounding the final accepted solution. The contoured surface was extended up to ± 2 times the values of *A, B,* and $S_c(Tg)$ to ensure that we had found the true minimum. Table 2 contains the optimal values obtained for each of the 4 datasets.

The original viscosity data and the best-fit curve for each of the four melt compositions are plotted in Figure 3A. We have also mapped the feasible solution space corresponding to the 95% confidence limits (e.g., Press et al. 1986, Russell et al. 2002;

Giordano et al. 2015). The confidence envelopes delineate the full range of parameter values (e.g., *A, B,* and S_c) that are equally valid descriptors of the experimental data at the specified confidence level (Figure 3B, C). The confidence limits also portray the magnitude and nature of covariances between model parameters (e.g. Russell et al. 2002).

The range of parameters (*A, B,* and S_c) reproducing the individual datasets is highly variable and depends on the number of viscosity measurements, their temperature distribution and their composition (e.g., *strong* vs *fragile*) (Fig. 3B, C) (Russell et al. 2002, 2003). The 2-D projections of the confidence ellipsoids (Figure 3B, C) are small for the anhydrous datasets because the viscosity measurements span a large range of temperatures. Conversely the hydrous melts allow for wide ranges in the model values of *A* (-7 to 2.5 Pa s), *B* (60 to 480 kJ mol^{-1}), and S_c (7.5 to 30.5 J mol^{-1} K^{-1}) (Table 2). The ability of the low-temperature viscosity data to constrain *A* is minimal. As would be expected, given the form of Eq. 3, the model-induced covariance is strongest between *B* and S_c(*Tg*). An additional consequence of the model is the negative covariance between *A* and *B* versus a positive covariance between *A* and S_c(*Tg*).

Subsequently, we have fit the AG equation (Eq. 4) to the same subset of data assuming these 4 melts share a common, but unknown, high-T limiting value to viscosity. We solve a single system of non-linear equations comprising the k=4 datasets by minimizing the function:

$$\chi^2_{min}(\boldsymbol{x}) = \sum_{j=1}^{k}\sum_{i=1}^{n_j}\left[\frac{log\ \eta_i - A - B_j/\left(T_i\left[S_{c,j} + Cp_{c,j}\ ln\left(\frac{T_i}{Tg_j}\right)\right]\right)}{\sigma_i}\right]^2 \qquad (6)$$

where $\boldsymbol{x}$ denotes the solution vector comprising a common value of *A*, and 2k values of *B*

and S_c, each. There are a total of 47 (Σn_j) observations of viscosity for the *k* melt compositions (Table 2). The objective function is weighted to uncertainties (σ_i) on viscosity arising from experimental measurement. We use the same solution techniques as described above and we use explicit differentiation of Eq. 6 to populate the (Σn_j x 2k+1) Jacobian matrix. The initial guess vector uses the average value of *A* and the values of *B* and S_c obtained for the individual datasets (Table 2).

The optimal parameters derived from simultaneous solution of the 4 datasets are summarized in Table 2 and Figure 4A. The original data are reproduced to within experimental uncertainty (+/- 0.25; Fig. 4B) and the optimal value of *A* for these 4 melt compositions is -2.29 +/- 0.6. The model values of *B* (90 - 208 kJ mol^{-1}) and S_c (6 - 19 J mol^{-1} K^{-1}) are substantially different from the values obtained for each melt independently and their range of values is substantially smaller (cf. Fig 3B, C *vs.* 4A). The reduced range for *B* and S_c values results from the 4 melts sharing a common value for *A*. The optimal values of *B* and S_c show a strong positive correlation as indicated by their 95% confidence ellipses (Fig. 4A) which is mainly a numerical or model-induced correlation owing to the nonlinear character of the AG function.

We have calculated the full range of acceptable AG functions based on the values of *B* and $S_c(Tg)$ defining the ellipses in Figure 4A. The solid lines denote the optimal fit to each set of viscosity measurements (Table 2). The dashed lines bounding the shaded fields in Figures 4C and 4D are the 2σ confidence limits on the model functions for each melt composition. In all four cases the family of curves consistent with the 2σ confidence limits (Fig. 4A) define narrow bands that are entirely consistent with the measurement

uncertainties on the original datasets. The experimental data allow a wide range of values of B and S_c, however, the strong correlation between parameters (Fig. 4A) controls how these values are combined. Thus, even though the hydrous melts allow a wide range of parameter values (Fig. 4A), they generate a narrow band of AG functions where there are experimental data.

Modelling of Anhydrous and Hydrous Melts

We have fit the AG model to the entire dataset of 50 anhydrous and hydrous melt compositions supported by 452 viscosity measurements. The optimization returns a single value for A and unique values of B and S_c for each melt. Model parameters are reported in Table 3 with corresponding calculated transport properties (e.g., Tg^{12}) and proxies for composition ($NBO/T_{hydrous}$ and $SM_{hydrous}$; Giordano et al. 2015; Giordano and Russell, 2016, this volume).

The optimization model constrains the value of A to -3.51 ± 0.25. This value is in excellent agreement with estimates (i.e. -4 to -5) from previous theoretical (Glastone et al. 1941; Myuller, 1955; Frenkel, 1959), experimental (e.g. Angell, 1985) and numerical studies (Russell et al. 2002; 2003). The model values of A depend to some extent on the functional form adopted to describe the temperature dependence of melt viscosity. For example, the values of A constrained by the AG equation versus the Vogel-Fulcher-Tammann (VFT) equation (Vogel 1921, Fulcher 1925, Tammann and Hess, 1926) typically differ by ~ one order of magnitude. For example, the high-T limits to melt viscosity for multicomponent silicate melts constrained by these two functions (AG *vs*. VFT) have a range of values of 10^{-3} -10^{-4} and 10^{-4} -10^{-5}, respectively (e.g., Russell et al. 2002; Giordano

and Russell, 2007).

The values of B and S_c for the 50 melt compositions (Fig. 5A) are strongly positively correlated having values of B and S_c ranging from ~130 - 450 kJ mol^{-1} and ~9 - 35 J mol^{-1} K^{-1}, respectively. Anhydrous and hydrous melts span virtually the same range of B and S_c values, however, hydrous melts are shifted to higher values of S_c or lower values of B. In addition, we observe that the most hydrous samples have the lowest values of B for the same S_c. Requiring the AG functions for all melt compositions to share a common value for A causes no significant reduction in the quality of fit to the viscosity measurements. As illustrated in Figure 5B, all data are reproduced to within experimental error. The largest deviations, which only slightly exceed +/- 0.25 log units, are restricted to the low temperature, high viscosity measurements on the hydrous melts (Fig. 5B)

Another measure of the integrity of this modelling is the capacity of the AG functions to predict properties that are implicit but independent of the original observations and measurements. The derivative properties that are computed from the model are melt fragility (m) and the calculated glass transition temperature (Tg^{12}). Here we calculate Tg^{12} as the temperature at which the model viscosity curve reaches a value of 10^{12} Pa s. This value of viscosity (i.e. 10^{12} Pa s) and its timescale of melt relaxation (~100 s) are chosen to match the measured values of Tg_{onset} which themselves depend on the cooling/heating rates employed during the DSC experiments (i.e. 10 K min^{-1}). The values of Tg^{12} are calculated using Eq. 3 by setting η to 10^{12} Pa s (e.g., Toplis et al. 1997; Toplis, 1998; Giordano and Russell, 2007; Webb, 2008):

$$Tg^{12}(K) = \frac{B}{(12 - A) \cdot S_c(Tg)} \quad . \quad (7)$$

Melt fragility (*m*) is a measure of the departure of melt viscosity from an Arrhenian T-dependence; strong Arrhenian-like liquids have low values of *m*, whereas higher *m* values correspond to increasing non-Arrhenian, fragile liquids (Angell, 1991, Angell et al. 2000). The kinetic melt fragility is represented by the steepness index (e.g. Plazek and Ngai, 1991; Böhmer and Angell, 1992; Toplis et al. 1997; Toplis, 1998; Rossler et al. 1998; Webb, 2008) and is calculated as:

$$m = \frac{B}{Tg^{12} \cdot S_c}\left[1 + \frac{C_p}{S_c}\right] \quad . \quad (8)$$

From Eq. 7, we can write 12-A = $B/(Tg^{12}\ S_c)$ (Toplis, 1997) and substitution into Eq. 8 yields:

$$m = [12 - A]\left[1 + \frac{Cp_c}{S_c}\right] \quad (9)$$

where the term [12 - A] is a constant for all silicate melts implying that *m* is proportional to Cp_c/S_c (cf. Toplis, 1997; Webb 2008).

The relationships between the model and calculated properties are explored graphically in Figure 6. There is little correlation between the measured values of Cp_c and the model values of S_c (Fig. 6A) although the anhydrous samples have lower values of S_c over the full range of Cp_c. There are two exceptions; the anhydrous pantellerite (PS_0) and Rocche Rosse rhyolite from Lipari (RR_Lipari) plot at substantially higher values of S_c. Notably, these two melt compositions have extremely low (< 0.1) NBO/T values and low fragilities (Table 3). There is no discernible pattern between relative H_2O content and Cp_c and S_c.

The predicted values of Tg^{12} from the AG functions (i.e. Eq. 7) agree well with the calorimetrically measured values of Tg_{onset} (Fig. 6B). Predicted values are within 15-25K

(Table 3) except for two anhydrous, strong melts HAB0 (Δ~80K) and R_R_Lipari (Δ~160K). The dry pantellerite (PS_0), which had a relatively high S_c value, agrees to < 5K. The capacity of the model curves to predict the DSC measured values of Tg_{onset} is strong support for the quality of the overall model (Fig. 6B). Calculated values of Tg^{12} and *m* are plotted in Fig. 6C. The anhydrous melts span a range of fragilities (20 - 57) and *Tg*'s (800-1100K). For the same range of melt fragility, the hydrous melts have uniformly lower predicted values of Tg^{12}. Increasing melt fragility corresponds to higher values of *Cpc/Sc* (Eq. 9). As noted by Giordano et al (2008), the fragility for hydrous melts appears to decrease weakly with increasing H_2O content (Fig. 6C).

Discussion

Fragility, Tg^{12}, Cp_c and S_c

Equation 9 carries substantial implications for the relationships between a transport property (*m*) and thermodynamic properties of the melt Cp_c and S_c (Toplis et al. 1997; Toplis, 1998; Webb, 2008). For example, Toplis et al. (1997) showed that melt fragility was controlled not only by Cp_c but also by S_c and suggested that more fragile melts featured higher Cp_c or lower S_c or both.

These relationships are illustrated in Figure 7 where values of *m* and S_c are contoured for Cp_c (Eq. 9). At constant values of Cp_c, melt fragility is proportional to $1/S_c$ (Eq. 9) and, thus, decreases nonlinearly with increasing S_c (Fig. 7A). Hydrous melts are shifted to higher values of S_c and lower *m* and tend to fall on higher contours of Cp_c. For a perfectly strong melt having no measurable change in configurational heat capacity ($\Delta Cp_c \sim 0$) the limit to *m* is 12-A which, here, is predicted as 15.51 (Fig. 6C). Similarly, as S_c

increases to values much greater than Cp_c fragility is also predicted to converge to 12-A.

These relationships are also expressed in Figure 7B where fragility is plotted against Cp_c and contoured for values of S_c (Eq. 9). The contours are linear (Eq. 9), a result of a common A, and have unique slopes ([12-A]/ S_c) whilst sharing a common intercept (12 -A). Most anhydrous melts have S_c values between 10 and 15, whilst hydrous melts span the full space and reach values greater than 30. As shown graphically, fragility will converge to [12-A] as Cp_c approaches 0 or as S_c approaches infinity.

These relationships suggest a highly useful plot of fragility *vs*. the ratio Cp_c/S_c for checking the internal consistency of models such as these. Equation 9 requires values *m* and Cp_c/S_c to define a single linear trend where the slope and intercept have the exact same value: [12-*A*]. In the case of our model, the data (Fig. 7C) are completely described by a line with slope and intercept of 15.51. This specific linear relationship is a consequence of adopting a common (unknown) high-temperature limit to melt viscosity (i.e. *A*) and using the complete data set to solve for the optimal value of *A*.

Also plotted on Figure 7C are data and a trendline from Webb (2008) who measured calorimetric and viscosity values for a series of SiO_2-Al_2O_3-Na_2O-CaO glasses. Webb's (2008) measurements of viscosity were all made at low temperatures close to *Tg*. However, noting that Toplis et al.'s (1997) optimizations of the Ab, Ne and Jd melts yielded a narrow range of individual *A* values, Webb (2008) adopted a single averaged value for *A* (-2.61) for her modelling. The consequence of this is portrayed in Figure 7C. The actual data points of Webb (2008) are shown as squares and a linear trendline is drawn through that dataset. The slope and intercept to her best fit trend line are not equal and this indicates that her solution is inconsistent with the concept of a common value of A for these melts. To demonstrate

this inconsistency further, we have plotted a model line that would be defined for a constant value of *A* of -2.61 (as adopted by Webb, 2008). This is represented by the dashed line which has slope and intercept of -2.61. The inconsistency in Webb's (2008) analysis is that she correctly adopted the idea of a common high temperature limit to melt viscosity but the value she adopted, arbitrarily from Toplis et al. (1997), was inconsistent with her data. Webb (2008) did speculate on the consequences of adopting different values of *A* for modelling these melts and glasses. She noted that a different *A* value resulted in the same trends between B and S_C but with different absolute values. For example, an A value of -4.5, instead of -2.6, caused values of B and S_C to increase by a factor of 1.2 - 1.5 and the ratio B/S_C to increase by 10-15%.

These relationships between Tg^{12}, *m*, and Cp_c/S_c are explored further in a 3-dimensional plot (Figure 8) in which are shown the model values for all 50 anhydrous (black symbols) and hydrous (light symbols) melt compositions. Visually, the data are constrained to a single plane which we have independently fitted as:

$$\frac{Cp_c}{S_c} = -\frac{Tg^{12}}{243399} + \frac{m}{15.518} - 0.996 \quad . \qquad (10)$$

The coefficients 243399, 15.518, 0.996 correspond well to the average value of *B* for all melts (i.e. 241276; $\Delta < 1\%$), the value of [*12-A*] (i.e. 15.51) and to 1, respectively (see Eq. 9). The diagram illustrates more clearly the relationships between these 3 model parameters for dry *vs*. hydrous melts. Hydrous melts have lower Tg^{12} and the most H_2O-rich melts have lower fragility implying that increasing water content tends to make the melts more Arrhenian (Giordano et al. 2008). For a fixed value of Cp_c/S_c, fragility is determined but Tg^{12} is unconstrained. For a fixed Tg^{12}, the melt fragility and Cp_c/S_c are linearly dependent

(Fig. 7C).

Compositional Controls

The compiled database spans a wide range of melt compositions (Fig. 1) which ultimately control the values of the model parameters (B and S_c). Figure 9 represents a preliminary exploration of how melt composition correlates with the ratio B/S_c which approximates the potential energy barrier to viscous flow (e.g., Toplis, 1998; Webb, 2008). The ratio is plotted against proxies for melt composition including mole fraction of SiO_2 and $NBO/T_{hydrous}$ and $SM_{hydrous}$; all three are computed on a hydrous basis (Giordano et al. 2015).

Anhydrous melts have higher B/S_c values than hydrous melts and increase with increasing SiO_2 content and decrease with increasing $NBO/T_{hydrous}$ and $SM_{hydrous}$. The decrease in B/S_c with the addition of network modifiers is ~10% at most for anhydrous melts. The B/S_c values of hydrous melts show substantially stronger patterns with respect to these compositional parameters. Universally, increasing H_2O content correlates with lower B/S_c values (e.g., Whittington et al. 2009; Giordano et al. 2015). Weakly hydrated melts show a slight (~10%) decrease in B/S_c relative to their anhydrous equivalents. However, melts with higher water contents show a strong (> 50%) systematic decrease in B/S_c and a concomitant rise in $NBO/T_{hydrous}$ and $SM_{hydrous}$ consistent with increasing depolymerisation. The patterns of decreasing B/S_c values with increased H_2O content are distributed across a range of SiO_2 contents, and $NBO/T_{hydrous}$ and $SM_{hydrous}$ values set by their anhydrous counterparts.

GRD Model Comparison

The modelling presented here uses the AG equation for representing the temperature dependence of melt viscosity (Eq. 3). An alternate function for capturing the non-Arrhenian temperature dependence of silicate melts is the Vogel-Fulcher-Tammann (VFT) equation (Vogel 1921, Fulcher 1925, Tammann and Hess, 1926). Both, the AG and VFT equations are effective descriptors of Arrhenian and non-Arrhenian viscosity over the temperature and compositional range of most geochemically-relevant melts and compositional proxies (Bottinga et al. 1995; Hess and Dingwell, 1996; Baker, 1996; Russell et al. 2003; Giordano and Russell, 2007; Avramov 2012).

The two functions model the T-dependence of silicate melts equally well and the corresponding model parameters (e.g., A_{VFT}, B_{VFT}, C_{VFT} *vs.* A_{AG}, B_{AG}, $S_{c\,AG}$) are equivalent under some conditions (Bottinga et al. 1995; Toplis, 1997; Giordano and Russell, 2007). However, the model values of the resulting parameters are usually significantly different. As discussed earlier, the *A* parameter representing the high-T limit to viscosity usually differs by ~1 log unit (e.g., A_{VFT} ~ -4.5 *vs*. A_{AG} ~ -3.5) for the same dataset. For a more complete analysis of the equivalence between the parameters derived from the 2 functions the reader is referred to Richet (1984), Bottinga et al. (1995), Richet and Bottinga (1995), Sipp and Richet (2002), and Giordano and Russell (2007***)***.

Giordano et al (2008) developed a model (GRD model) for predicting the viscosity of multicomponent natural silicate melts as a function of T and melt composition, including volatile constituents. Their model used the VFT equation for the T-dependence and their common, high-T limit on viscosity (A_{VFT}) was ~ -4.6. The main attributes of the GRD model are its ability to predict: i) the viscosity of natural volatile-bearing silicate melts, in a continuous manner, across composition- and temperature-space; and to predict ii) other

transport properties including glass transition temperatures ($Tg^{12}{}_{VFT}$) and melt fragility (m_{VFT}).

Below we have compared the values of $Tg^{12}{}_{AG}$ and m_{AG} predicted by the AG modeling of viscosity presented here (Eq. 7 and 9, respectively) to the corresponding values predicted by the GRD model. Values of $Tg^{12}{}_{VFT}$ are calculated using the GRD model from:

$$Tg^{12}{}_{VFT} = \frac{B_{VFT}}{[12 - A_{VFT}]} + C_{VFT} \qquad (11)$$

and, similarly, fragility (m_{VFT}) is calculated as:

$$m_{VFT} = \frac{B_{VFT}}{Tg^{12}{}_{VFT}\left(1 - {C_{VFT}}/{Tg^{12}{}_{VFT}}\right)^2} \quad . \qquad (12)$$

Figure 10 shows the values predicted for the 50 melt compositions in our database (Tables 1, 3, A1). The values of Tg^{12} predicted by our AG model *versus* the GRD model based on Eq. 7 and 11 (Table 3) show remarkable agreement. A total of 13 compositions have differences > 50K. These are the peralkaline and phonolite melts in our database and these melts were poorly represented in the original calibration of the GRD model. Three melt compositions have differences > 100K including two anhydrous synthetic melts (An100, HAB0) and a single hydrous phonolite. Furthermore, both models systematically predict higher values of Tg^{12} for the anhydrous melts and lower values for the hydrous melts that are proportional to H_2O content.

Calculated values of fragility show some scatter (Fig. 10B). However, the overall agreement is substantially better than the scatter might suggest as only 6 compositions have fragility differences exceeding 10. The anhydrous melts show very good agreement (± 6%) and cover a full range of *m* values (2 - 55). The most hydrous melts correspond to the

lowest values of fragility regardless of which model is used. If we use m ~30 as a cutoff between stronger and more fragile silicate melts, Figure 10B shows that both models predict the *relative* fragility of the melts very well. The only exceptions are 3 hydrous trachybasalt melts which would be viewed as strong using the AG model and more fragile by the GRD model. Notably, the AG model for these 3 melts is based on a relatively small, number of low temperature viscosity measurement meaning that their fragility is poorly constrained by the data (e.g., 800-1, N=4; 801-1, N=6; 802-1, N=3).

In the above analysis we are comparing properties that are implicit to two different models; but both models are constrained by measured values of viscosity. One last means of comparison is to use the GRD model, which is only constrained by measurements of melt viscosity, to calculate the implied thermodynamic properties. We use the GRD model to calculate the ratio Cp_c/S_c as a derivative property for the 50 melt compositions listed in Table A1 (Table 3) from:

$$\left[\frac{Cp_c}{S_c}\right]_{VFT} = \frac{m_{VFT}}{[12 - A_{VFT}]} - 1 \quad . \qquad (13)$$

The comparison of Cp_c/S_c values derived from the AG and VFT models is shown in Figure 10C. The pattern is very similar to that observed for the fragility values calculated from the two models. However, there is one interesting point that illustrates the consistency between these two models for melt viscosity. The predicted values of Cp_c/S_c fall into two groups: melts where $Cp_c/S_c \leq 1$ *vs.* melts having values > 1. In the former, configurational entropy plays a major or equal role relative to configurational heat capacity. In the latter group configurational heat capacity dominates. In terms of predicting the overall roles of Cp_c and S_c, the two models agree very well. This is a remarkable concordance given the fact that,

for the AG model, Cp_c is measured and S_c is recovered directly as one of adjustable parameters for each melt whilst, for the VFT function (i.e. GRD model), the ratio is calculated from the values of A_{VFT}, B_{VFT} and C_{VFT} predicted independently on the basis of melt composition alone.

Summary

The Adam-Gibbs theory describes the temperature dependence of melt viscosity and offers a means of connecting the transport and thermochemical properties of melts. The connection arises because both viscosity and calorimetric properties are controlled by the melt's structural configuration. To develop a composition-dependent model for viscosity using the Adam-Gibbs theory requires an understanding of how the parameters B and $S(T)$ vary with composition (Eq. 1). Ideally, the compositional basis would reflect the structural properties of the melt. However, in order to separate the individual behaviour of these two adjustable parameters requires measured values of heat capacity across the glass transition.

Over the last decade, the database of viscosity and calorimetric measurements on individual multicomponent natural and synthetic silicate melts has increased substantially. We have taken advantage of these published datasets to model the temperature-dependent viscosity of 50 anhydrous and hydrous silicate melts with the Adam-Gibbs equation (Eq. 2). Our optimization follows established strategies with the exception that we assume that all melts converge to a common high-temperature limiting value represented by the parameter A (Eq. 2).

Our optimization solves for a single value of A for all 50 melts, thereby, reducing the total number of adjustable parameters. Our model fit reproduces the entire dataset to

within experimental error and there is no significant decrease in the quality of fit to the data. Two other attributes of this approach are that it provides estimates of B and $S_c(Tg)$ that are not correlated to variations in values of A, and it allows us to incorporate datasets where the number of viscosity measurements are few or made only at low temperature. Lastly, it means that all compositional dependencies are consigned to B and $S_c(Tg)$.

The optimal value of A for this dataset is -3.51 which is a value that agrees well with theoretical and experimental based values established for silicate and organic glass - melt systems described by the Adam-Gibbs model. We recommend that this value be adopted when the temperature dependence of viscosity is being modelled using the Adam-Gibbs equation. Our model returns estimates of $S_c(Tg)$ for a range of silicate melts and our analysis has established a unique plane defined by the ratio of Cp_c/S_c, melt fragility (m) the and the glass transition temperature (Tg^{12}). The plane provides a direct connection between the thermodynamic properties of multicomponent silicate melts (Cp_c/S_c) and properties derived from the temperature dependence of melt viscosity.

Acknowledgments

This research was supported by the Natural Sciences and Engineering Research Council of Canada through the Discovery Grants and Discovery Accelerator Supplements programs (J.K. Russell) and research funds (2012-2015) provided by the University of Turin (D. Giordano).

References Cited

Adam G & Gibbs JH (1965) On the temperature dependence of cooperative relaxation properties in glass-forming liquids. Journal of Chemical Physics 43, 139–146.

Angell CA (1985) Strong and fragile liquids. in Ngai KL and Wright GB (eds.) Relaxations in complex systems. U.S. Department of Commerce National Technical Information Service, Springfield, Virginia, pp. 3-11.

Angell CA (1991) Relaxation in liquids, polymers and plastic crystals - strong/fragile patterns and problems. J. Non-Crystalline Solids, 131-133, 13-31.

Angell CA, Ngai KL, McKenna GB, McMillan PF & Martin SW (2000) Relaxation in glassforming liquids and amorphous solids. J. Applied Physics 88, 3113-3149.

Avramov I (2013) The role of entropy on viscosity of silicates. J. Non-Crystalline Solids 362, 120-123.

Baker DR (1996) Granitic melt viscosities: Empirical and configurational entropy models for their calculation. Am. Min. 81, 126-134.

Böhmer R and Angell CA (1992) Correlations of the nonexponentiality and state dependence of mechanical relaxations with bond connectivity in Ge-As-Se supercooled liquids. Phys. Rev. 45, 10091–10094.

Bottinga Y & Richet P (1996) Silicate melt structural relaxation; rheology, kinetics, and Adam Gibbs theory. Chem. Geol. 128, 129-141.

Bottinga Y, Richet P, & Sipp A (1995) Viscosity regimes of homogeneous silicate melts. Am. Min. 80, 305-319.

Bouhifd MA, Whittington A, Roux J, & Richet P (2006) Effect of H_2O on the heat capacity of polymerized aluminosilicate glasses and melts: Geochim Cosmochim Acta 70, 711–722.

Bouhifd MA, Whittington A, Withers AC, & Richet P (2013) Heat capacities of hydrous silicate glasses and liquids. Chem. Geol. 346, 125 - 134.

Di Genova D, Romano C, Giordano D, & Alletti M (2014) Heat capacity, configurational heat capacity and fragility of hydrous magmas. Geochim Cosmochim Acta 142, 314 - 333.

Dingwell DB (1995) Relaxation in silicate melts: Applications. *In* (Eds. JF Stebbins, PF McMillan, DB Dingwell) Structure, Dynamics & Properties of Silicate Melts, Reviews in Mineralogy 32, 21-66.

Dingwell DB & Webb SL (1989) Structural relaxation in silicate melts and non-Newtonian

melt rheology in geologic processes. Phys. Chem. Minerals 16, 508-516.

Eyring H, Henderson D, Stover BJ, & Eyring EM (1982) Statistical Mechanics and Dynamics, John Wiley, Second edition, NY, 1982. 785 pp.

Frenkel YI (1959) The kinetic theory of liquids. Slected works vol 3 (Moscow-Leningrad: Izd. Akad. Nauk SSSR)(in Russian)

Fulcher GS (1925) Analysis of recent measurements of the viscosity of glasses. Am. Ceramic Soc. 8, 339-355.

Giordano D, Russell JK (2007) A rheological model for glassforming silicate melts in the systems CAS, MAS, MCAS. J. Phys. Condensed Matter 19: 205148

Giordano D & Russell JK (2016) The heat capacity of hydrous multicomponent natural melts and glasses. Chem. Geol. This volume.

Giordano D, Nichols ARL, Potuzak M, Di Genova D, Romano C, & Russell JK (2015) Heat capacity of hydrous trachybasalt from Mt Etna: comparison with CaAl2Si2O8 (An)–CaMgSi2O6 (Di) as basaltic proxy compositions. Contrib. Min. Petrol. 170, 48, DOI 10.1007/s00410-015-1196-6.

Giordano D, Russell JK, & Dingwell D (2008) Viscosity of magmatic liquids: A model. Earth Planet. Sci. Lett. 271, 123-134.

Glastone S, Laidler KJ, Eyring H (1941) The theory of rate processes. McGraw-Hill, New York.

Hess KU & Dingwell DB (1996) Viscosities of hydrous leucogranitic melts: A non-Arrhenian model. Am. Min. 81, 1297-1300.

Jensen M & Jakobsen J (2015) Configurational entropy in thermoset polymers. J. Phys. Chem., Part B, 119, 5645–5649.

Myuller RL (1955) A valence theory of viscosity and fluidity for high-melting glass-forming materials in the critical temperature range. Zhurnal Prikladnoi Khimii 28, 1077–1087.

Plazek DJ and Ngai KL (1991) Correlation of polymer segmental chain dynamics with temperature-dependent time-scale shifts. Macromolecules 24, 1222–1224.

Press WH, Flannery BP, Teukolsky SA, Vetterling WT (1986) Numerical Recipes: the Art of Scientific Computing. Cambridge University Press, Cambridge, 818 p.

Richet P (1984) Viscosity and configurational entropy of silicate melts. Geochimica et Cosmochimica Acta, 48, 471-483.

Richet P & Bottinga Y (1986) Thermochemical properties of silicate glasses and liquids: A review. Rev. Geophys. 24, 1-25.

Richet P & Bottinga Y (1995) Rheology and configurational entropy of silicate melts. *In* (Eds. JF Stebbins, PF McMillan, DB Dingwell) Structure, Dynamics & Properties of Silicate Melts, Reviews in Mineralogy 32, 67-94.

Richet P & Neuville DR (1992) Thermodynamics of silicate melts: Configurational properties. *In* (Ed. S Saxena) Advances in Physical Geochemistry 10, 132-161.

Richet P & Toplis MJ (2001) Thermodynamic aspects of the glass transition of silicates. Physics of Glasses, C. R. Acad. Sci. Paris, t. 2, Série IV, 191–202.

Robert G, Whittington AG, Stechern A, & Behrens H (2014) Heat capacity of hydrous basaltic glasses and liquids. J. Non-Cryst. Solids 390, 19–30.

Rossler E, Hess KU, and Novikov VN (1998) Universal representation of viscosity in glass forming liquids. J. Non-cryst. Solids 223, 207–222.

Russell JK, Giordano D, Dingwell DB, & Hess K-U (2002) Modelling the non-Arrhenian rheology of silicate melts: Numerical considerations. European J. Mineral. 14, 417–427.

Russell JK, Giordano D, & Dingwell D (2003) High-temperature limits on viscosity of non-Arrhenian silicate melts. Am. Min. 88, 1390-1394.

Russell JK & Giordano D (2005) A model for silicate melt viscosity in the system $CaMgSi_2O_6$-$CaAl_2Si_2O_8$-$NaAlSi_3O_8$. Geochimica Cosmochimica Acta 69, 5333-5349.

Solvang M, Yue Y-Z, Jensen SL & Dingwell DB (2005) Rheological and thermodynamic behavior of calcium aluminosilicate melts within the anorthite– wollastonite–gehlenite compatibility triangle. J. Non-Cryst. Solids 351, 499–507.

Toplis MJ (1998) Energy barriers to viscous flow and the prediction of glass transition temperatures of molten silicates. Am. Min. 83, 480–490.

Toplis MJ, Dingwell DB, Hess K-U & Lenci T (1997) Viscosity, fragility and configurational entropy of melts along the join SiO_2-$NaAlSiO_4$. Am. Min. 82,

979-990.

Webb SL (2008) Configurational heat capacity of Na2O–CaO–Al2O3–SiO2 melts. Chem. Geol. 256:92–101

Whittington AG, Bouhifd MA, & Richet P (2009) The viscosity of hydrous $NaAlSi_3O_8$ and granitic melts: Configurational entropy models. Am. Min. 94, 1-16.

Figure Captions

Figure 1. Measured properties of silicate melts in this study. Anhydrous melts are shown as filled black symbols and hydrous melts as grey circles. In all figures the size of grey symbols denotes the relative H_2O contents of the hydrous melts. (A) Chemical compositions of 50 experimental melts represented as Wt. % SiO_2 versus Na_2O + K_2O. (B) Calorimetrically-measured values of temperature marking the onset to Tg (Tg_{onset}) versus the temperature of the fully relaxed melt (Tg_{melt}). (C) Measured values of configurational heat capacity (Cp_c) plotted as a function of composition (SiO_2). (See Figure A1 for details).

Figure 2. Compilation of high-temperature measurements of melt viscosity on anhydrous (black symbols) and hydrous (grey symbols) used in this study and plotted as log η *vs*. 10000/T(K). Data includes 452 measurements on 50 anhydrous and hydrous melt compositions spanning a temperature range of 585 - 2450 K (Table 1).

Figure 3. Model fits to data for 4 individual melt compositions including anhydrous and hydrous phonolite (Phon) and basalt (Etn) (Table 2). (A) The distribution of data compared to best fits based on unique values of *A*, *B* and S_c for each composition. (B) The 2σ solution space for the Adam-Gibbs equation fitted to each of the datasets. The 95% confidence envelopes on the solution are shown as 2-D slices through the corresponding 3-D confidence ellipsoids for the optimal parameters *A*, *B* and S_c projected onto the *A vs*. *B* plane (at fixed S_c). Solid dots represent optimal solution. (C) The 95% confidence limits of the optimal parameters *A*, *B* and S_c

projected onto the *A vs*. S_c plane (at fixed *B*). Solid dots denote the optimal solution.

Figure 4. Model fit to entire dataset (N=47) for 4 melt compositions shown in Figure 3 (e.g., hydrous and anhydrous Phon and Etn) assuming that each of the 4 datasets share a common (but unknown) value of *A* (Table 2). (A) Optimal solutions for 4 melts illustrated as confidence ellipses on the parameters S_c and *B*; optimal *A* is 2.29 +/- 0.6. (B) The model misfits ($\Delta \log \eta$) plotted against observed values of $\log \eta$ for the 4 melt compositions (47 data points). Grey shaded field denote □0.2 log units of viscosity. (C) The family of model curves (shaded fields bounded by dashed lines) for the anhydrous and hydrous Etn melt compositions based on 95% confidence limits shown in (A). (D) Model curves as in (C) for the anhydrous and hydrous Phon melt composition based on 95% confidence limits shown in (A). The permitted range of model curves ultimately reflects the number, the quality, and the distribution of data (Russell et al. 2002.

Figure 5. Results of fitting the Adam-Gibbs function to the entire viscosity dataset and assuming that all melts share a common, unknown high-temperature limiting value of $\log \eta$ (*A* = -3.51; Table 3). (A) Optimal values of S_c (J mol^{-1} K^{-1}) and *B* (kJ mol^{-1}) returned for each of the 50 anhydrous and hydrous silicate melt compositions. Symbols as in Figure 1. Predicted values of S_c and *B* vary from 9 - 37 J mol^{-1} K^{-1} and from 100 - 450 kJ mol^{-1}, respectively. (B) Measured values of viscosity are compared against model values. Dashed lines indicate ±0.25 uncertainty on values $\log \eta$.

Figure 6. Implicit properties derived from the Adam-Gibbs model applied to viscosity measurements on anhydrous and hydrous silicate melts and assuming a common value of *A* (-3.51). Symbols as in Figure 1. (A) Optimal values of S_c (Table 3) plotted against measured values of Cp_c (Table 1). (B) Calculated values of Tg^{12} (K), taken as the temperature corresponding to a model viscosity of 10^{12} Pa s (Table 3), plotted against the measured values of Tg_{onset}. (C) Calculated values of Tg^{12} (K) and

fragility (m) derived from Adam-Gibbs equation (Table 3) applied to the viscosity database (Table 1) and assuming a common A. Near vertical dashed line denote constant values of Cp_c/S_c (Eq. 9).

Figure 7. Model values of fragility (m_{AG}) compared to thermodynamic properties of the silicate melts. Symbols as in Figure 1. (A) Fragility plotted against model values of S_c and contoured for values of Cp_c. (B) Fragility plotted against measured values of Cp_c and contoured for values of S_c. (C) Fragility plotted against values of the ratio Cp_c/S_c. The consequence of a common high-temperature limit to silicate melt viscosity (i.e. common value of A) is that fragility is linearly dependent on Cp_c/S_c where the slope and intercept have the same value (12-A). Plotted for comparison are the data from Webb (2008), the approximate trend line from Webb's analysis and the appropriate model line prescribed by Webb's adoption of a value for A of -2.61. (See text for full discussion)

Figure 8. Model plane relating the ratio of thermodynamic configurational energies of silicate melts (Cp_c/S_c) to model values of melt fragility (m_{AG}) and glass transition temperature (Tg^{12}_{AG}). All values for the suite of anhydrous (black) and hydrous (blue) melts plot on a single unique plane (see text).

Figure 9. Correlation between model parameters (i.e. B/S_c) and compositional variables, including: (A) mole fraction SiO_2, (C) $NBO/T_{Hydrous}$, and (C) $SM_{Hydrous}$. Symbols as in Figure 1.

Figure 10. Comparison of properties derived from this Adam-Gibbs-based model (AG) and values calculated from the GRD model (Giordano et al. 2008). Model values include: (A) Tg^{12} (i.e. $\eta = 10^{12}$ Pa s), (B) Fragility (m), and (C) the ratio of thermodynamic properties (Cp_c/S_c). Symbols as in Figure 1.

Figure A1. An example heat capacity curve (Cp) derived from a differential scanning

calorimeter (DSC) experiment on a silicate glass showing how the different parts of the glass transition are defined. The *Cp* curve in the figure was generated after cooling and heating from the glassy state through the glass transition at 10 K min^{-1}. The thick grey line is the Maier–Kelley equation fit to the heat capacity data for the glass. The onset to the glass transition (Tg_{onset}) is defined here by the intersection of the extrapolated Maier-Kelley equation and a linear trend defined by the rapid rise in *Cp* prior to reaching a peak value (Tg_{peak}). Values of the calorimetric Tg_{melt} representing the first temperature corresponding to the fully relaxed melt are taken as flat portion of the *Cp* curve following the *Cp* peak. The configuration heat capacity (Cp_c) is defined by the difference in *Cp* values taken at these two temperatures (i.e. Tg_{onset} vs. Tg_{melt}). See Giordano et al. (2015) for more details.

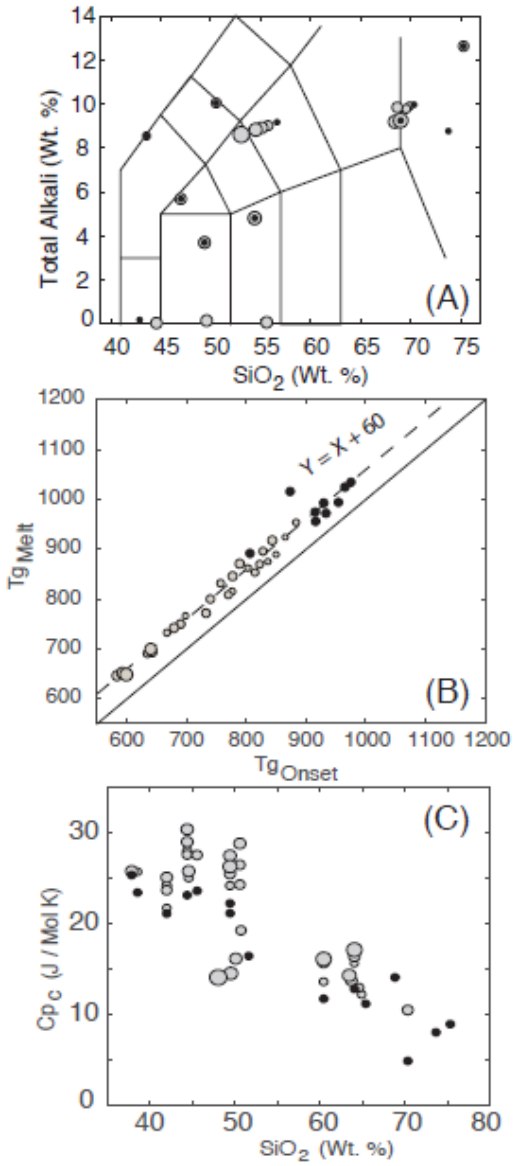

Figure 1: [Russell & Giordano, 2016; Chemical Geology]

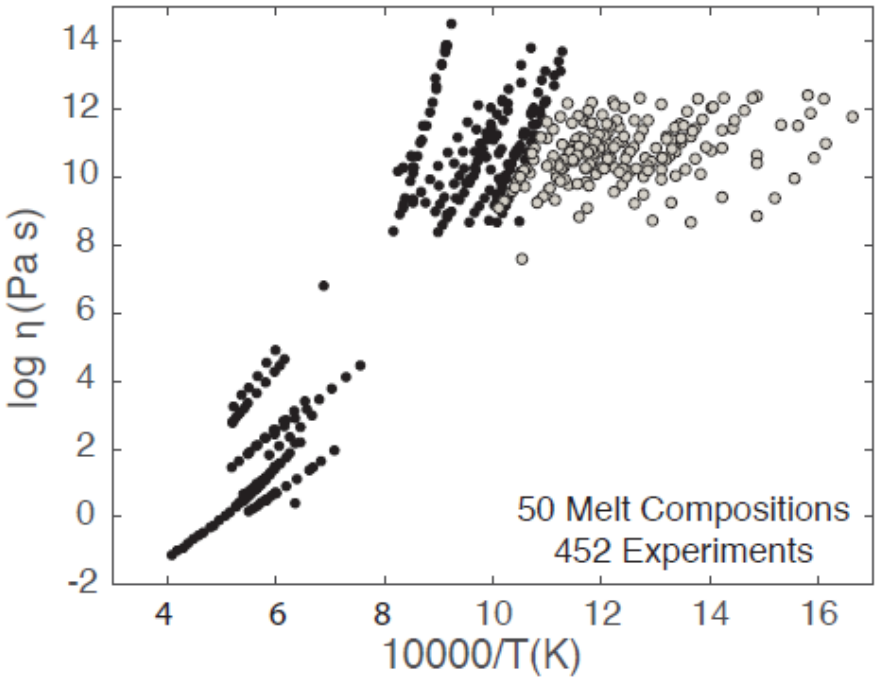

Figure 2: [Chemical Geology; Russell & Giordano 2016]

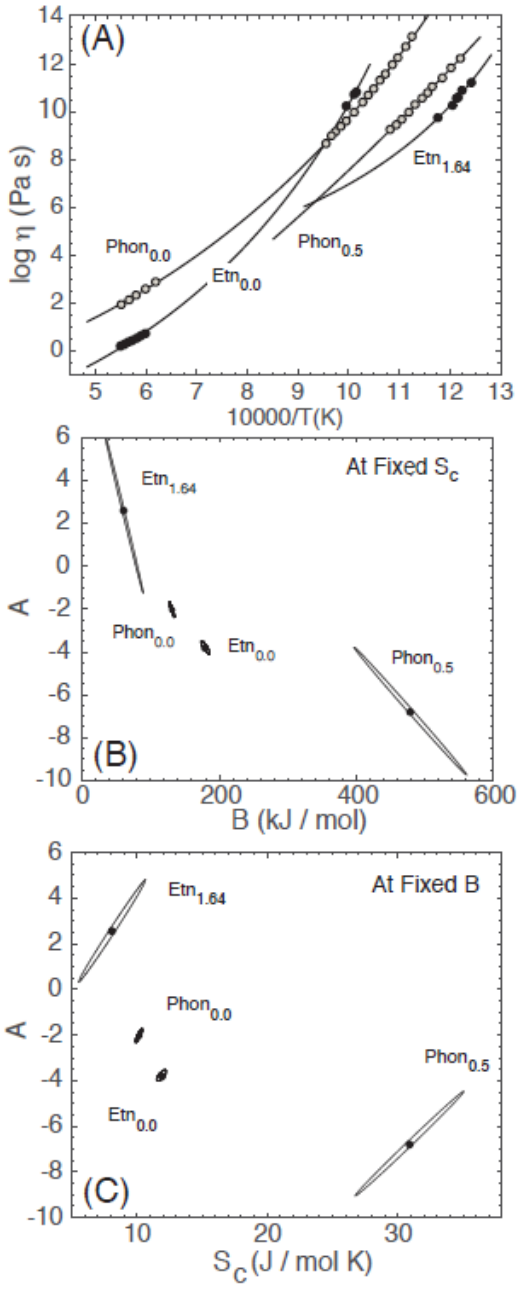

Figure 3. [Russell & Giordano, 2016; Chemical Geology]

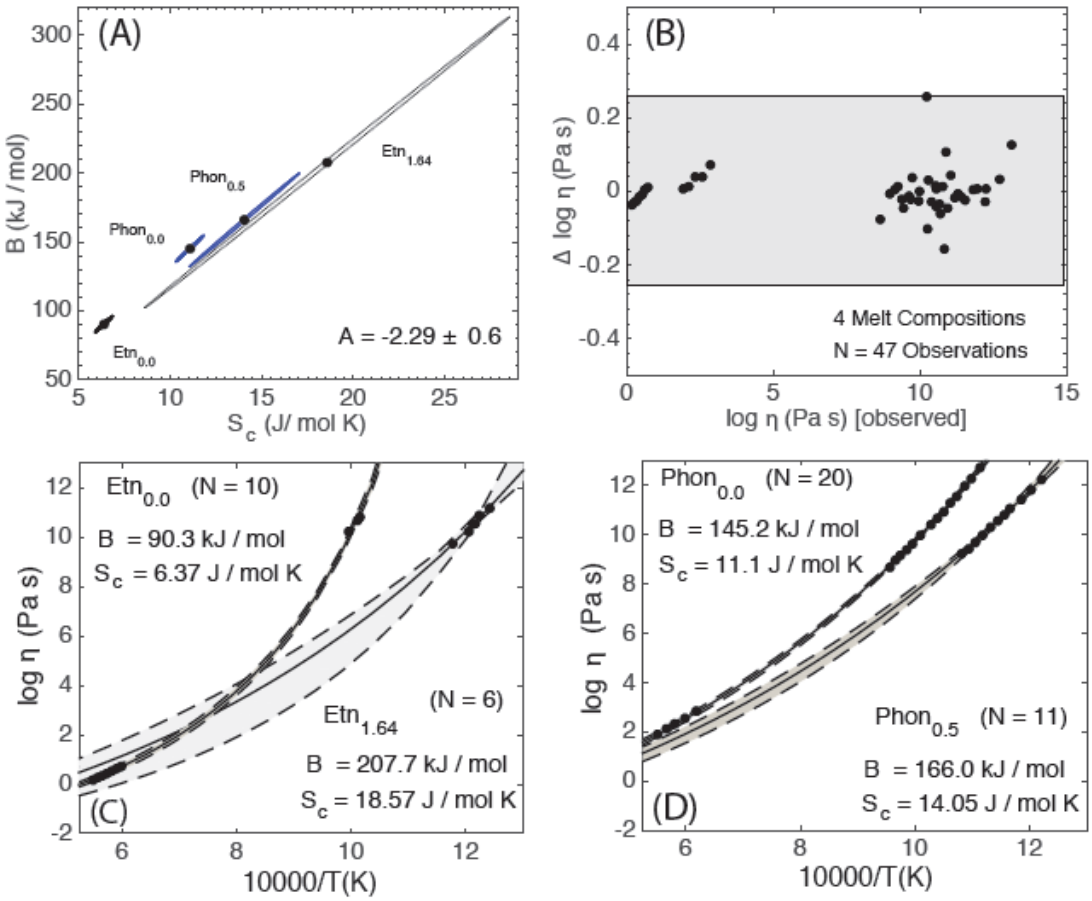

Figure 4. [Russell & Giordano, 2016, Chemical Geology]

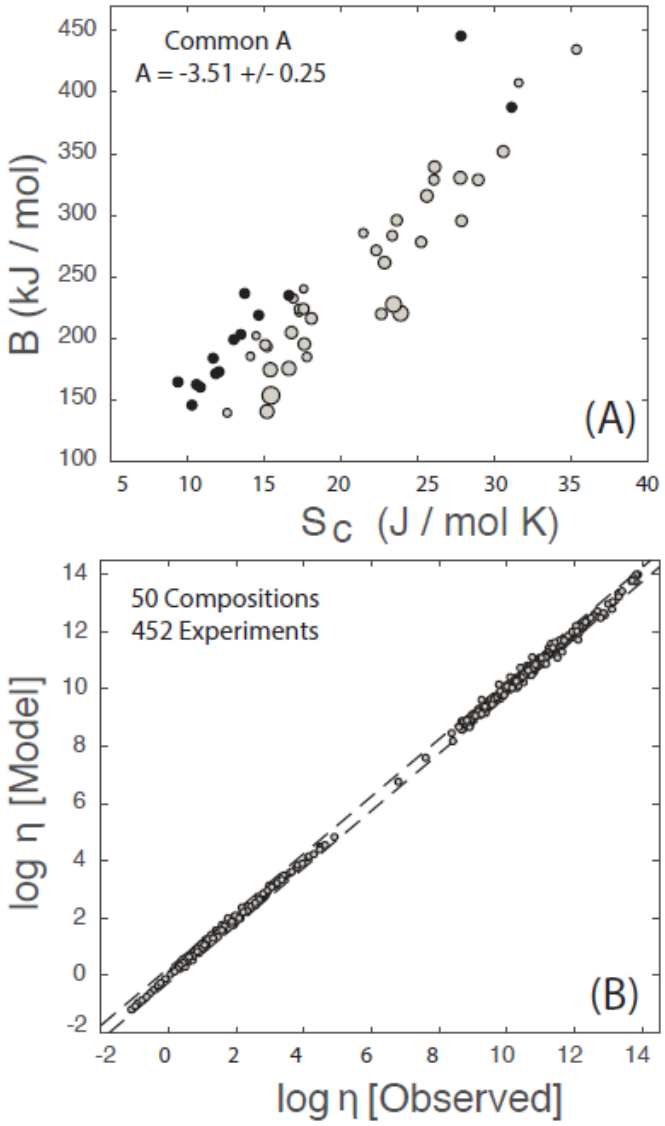

Figure 5 [Russell & Giordano, 2016; Chem Geol]

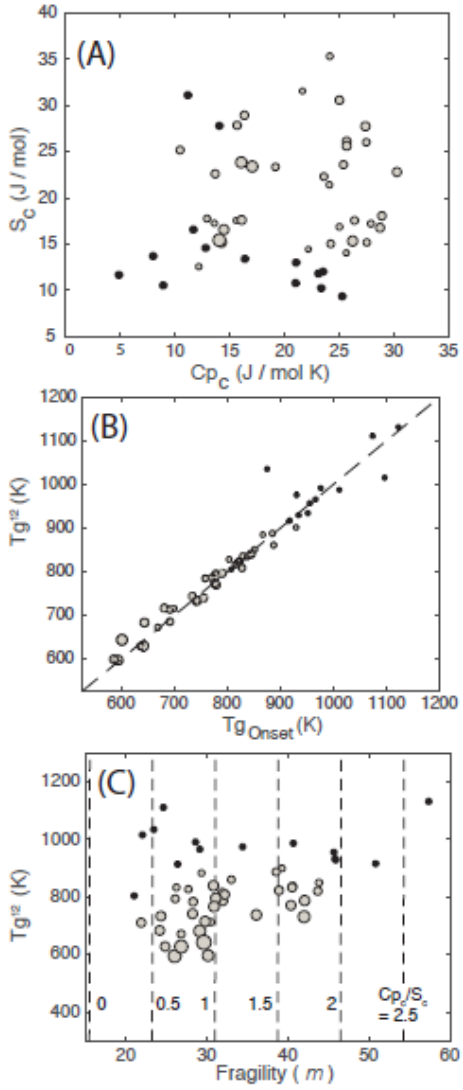

Figure 6 [Russell & Giordano, 2016; Chem Geol]

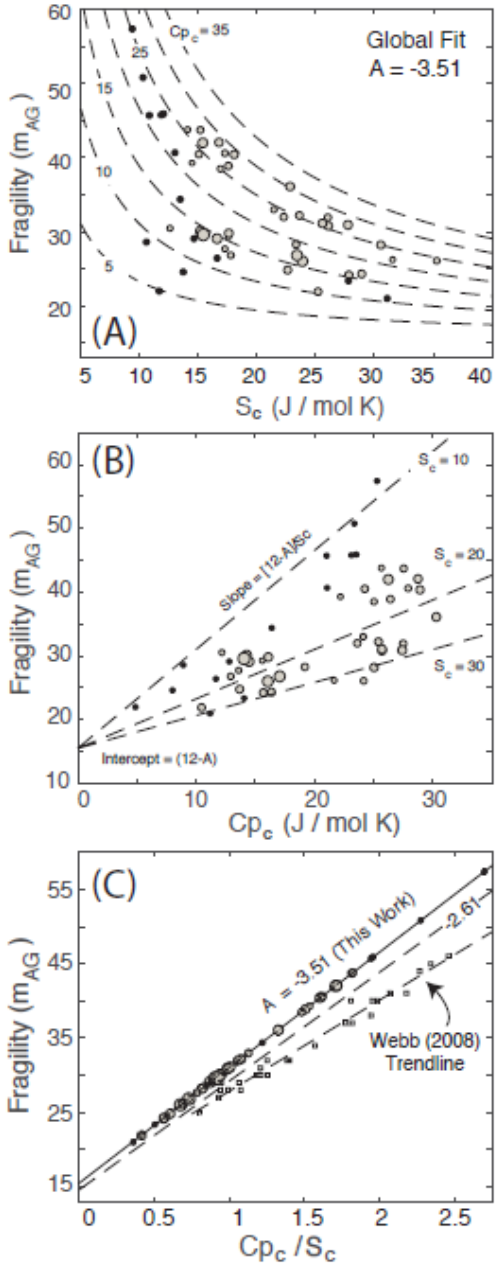

Figure 7 [Russell & Giordano, 2016; Chem Geol]

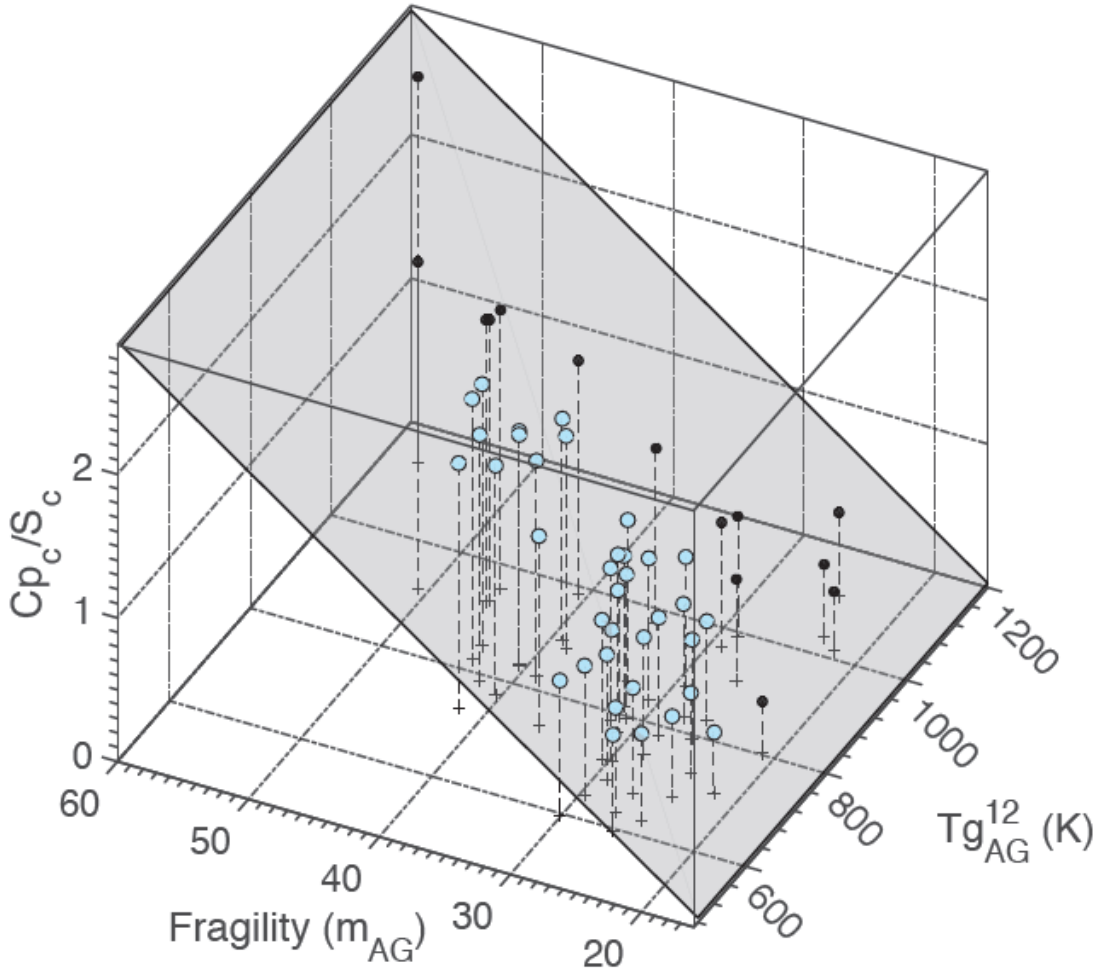

Figure 8 [Russell & Giordano, 2016; Chem Geol]

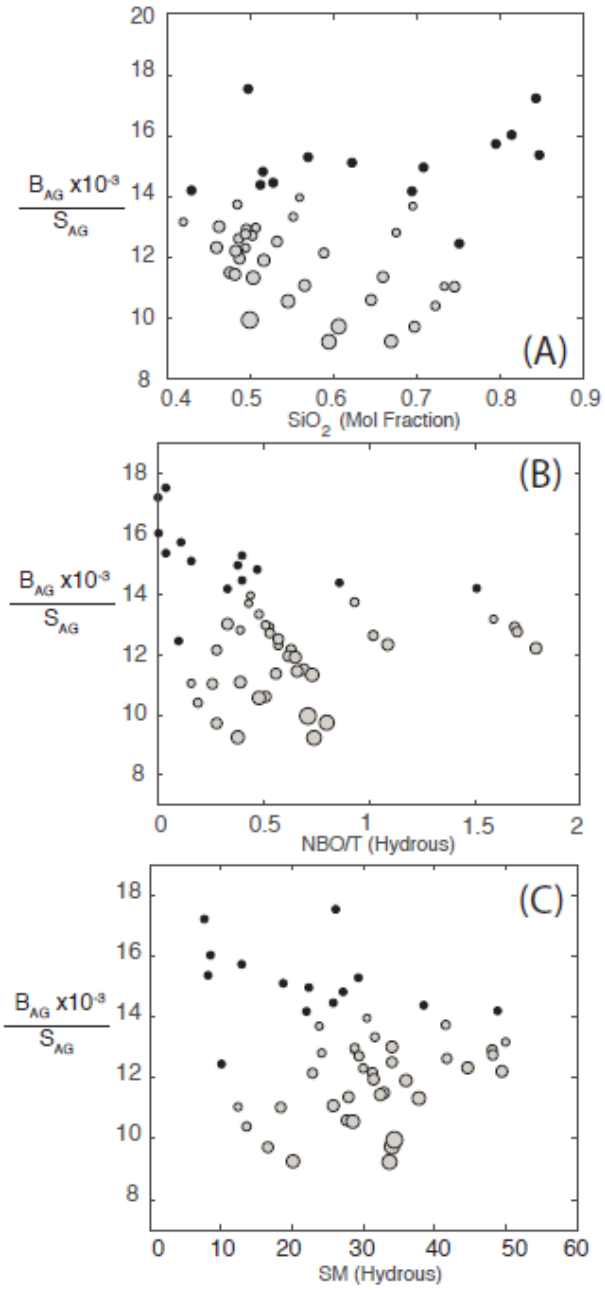

Figure 9 [Russell & Giordano, 2016; Chem Geol]

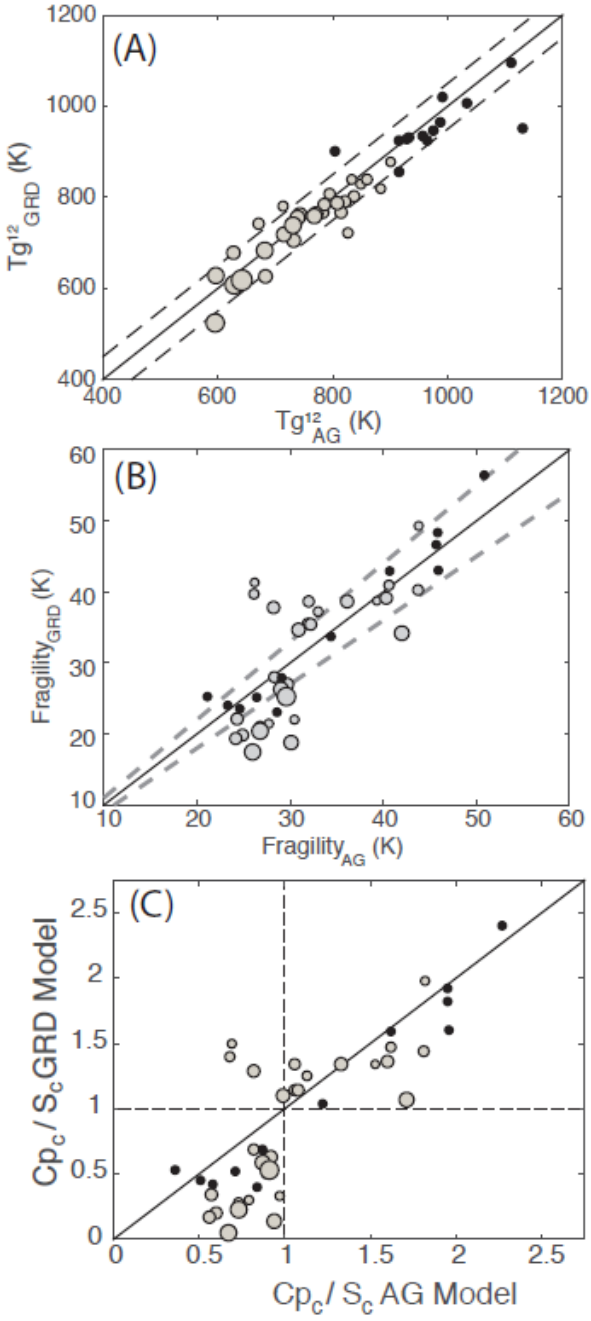

Figure 10 [Russell & Giordano, Chem Geol, 2016]

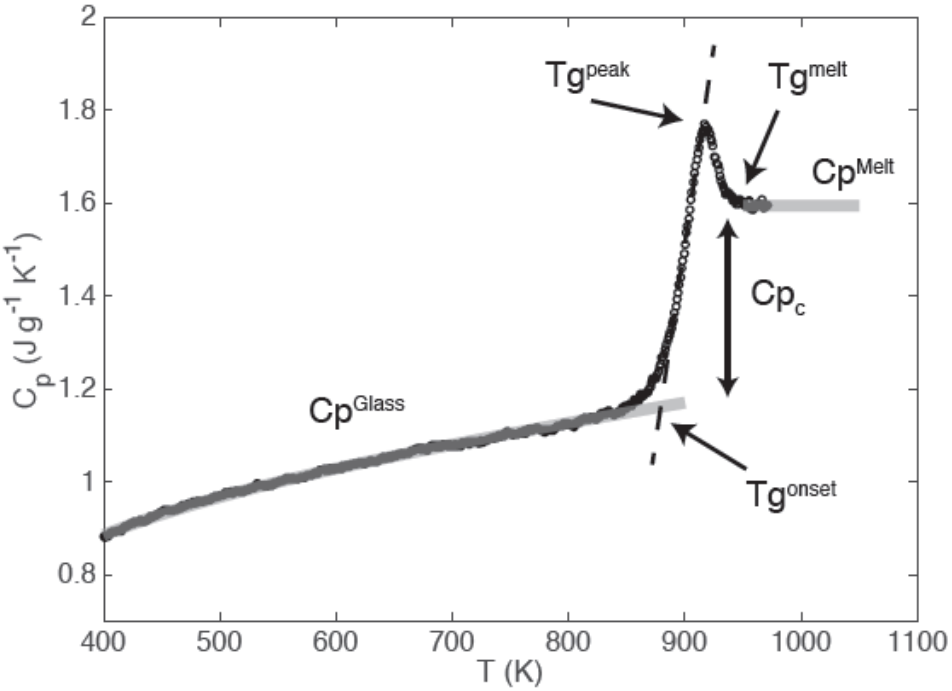

Figure A1. [Russell & Giordano, 2016; Chem Geol]

Table 1. Datasets having measured values for Cp_c, Tg_{onset}, and viscosity on the same melt compositions. Data include: melt composition (wt. %), number (N) of viscosity measurements, temperature interval of meaurements, and data sources.

No.	Composition	Label	SiO_2	H_2O	N	ΔT(K)	Tg_{onset}	Tg_{melt}	Cp_c	Source
1	Anorthite	An100_dry	42.90	0.00	66	1082-2449	1122	1183	25.29	Solvang et al. (2005)
2	An-Di	An10Di90H2	55.60	1.69	3	870-898	828	896	24.23	Giordano et al. (2015)
3	An-Di	An10Di90H3	55.60	1.75	3	854-949	822	870	26.42	Giordano et al. (2015)
4	An-Di	An10Di90H4	55.60	2.58	3	807-863	777	846	28.76	Giordano et al. (2015)
5	An-Di	An42Di58H1	49.60	1.05	3	900-945	883	954	25.02	Giordano et al. (2015)
6	An-Di	An42Di58H3	49.60	2.70	4	786-845	788	871	25.72	Giordano et al. (2015)
7	An-Di	An90Di10H2	42.90	2.56	4	861-896	843	918	25.72	Giordano et al. (2015)
8	Dacite	DK-89	80.25	0.00	14	934-1119	975	1035	8.93	Bouhifd et al. (2006)
9	Latite	FR_Dry	56.63	0.02	12	973-1499	929	993	16.40	Di Genova et al. (2014)
10	Latite	FR_1.6	55.74	1.59	4	793-853	757	832	19.20	Di Genova et al. (2014)
11	Latite	FR_2.7	55.12	2.69	5	713-783	679	742	16.20	Di Genova et al. (2014)
12	Latite	FR_3.8	54.51	3.76	3	673-713	641	695	14.50	Di Genova et al. (2014)
13	Latite	FR_6.3	53.06	6.32	3	633-673	599	649	14.00	Di Genova et al. (2014)
14	Pantellerite	PS_0	70.35	0.02	12	863-1673	806	892	11.10	Di Genova et al. (2014)
15	Pantellerite	PS 0.5	69.89	0.72	4	733-793	698	766	12.20	Di Genova et al. (2014)
16	Pantellerite	PS 1.1	69.56	1.16	4	703-773	666	733	12.90	Di Genova et al. (2014)
17	Pantellerite	PS 2.2	68.67	2.11	3	673-733	634	691	13.60	Di Genova et al. (2014)
18	Pantellerite	PS 3.5	68.43	3.55	4	628-673	583	647	14.30	Di Genova et al. (2014)
19	Phonolite	Phon-0.0	65.40	0.00	20	889-1816	915	975	11.68	Bouhifd et al. (2006)
20	Phonolite	Phon_0.5(B)	65.40	0.78	11	819-925	802	862	13.59	Bouhifd et al. (2006)
21	Phonolite	Phon_2.2	65.40	2.15	8	676-748	690	750	15.67	Bouhifd et al. (2006)
22	Phonolite	Phon_5	65.40	4.72	3	587-620	592	652	16.06	Bouhifd et al. (2006)
23	Tephrite	NIQ_0	43.57	0.00	20	886-1573	916	956	23.36	Bouhifd et al. (2013)

24	Tephrite	NIQ_0.68	43.57	0.68	7	845-888	850	890	25.66	Bouhifd et al. (2013)
25	Tephrite	Teph_Dry	50.56	0.00	22	918-1719	933	973	23.54	Bouhifd et al. (2013)
26	Tephrite	Teph_1.5	50.56	1.60	3	816-847	814	854	27.49	Bouhifd et al. (2013)
27	Trachybasalt	Etn_0	47.03	0.02	10	985-1818	954	994	21.05	Giordano et al. (2015)
28	Trachybasalt	801-1	47.03	0.64	6	848-893	836	876	21.66	Giordano et al. (2015)
29	Trachybasalt	800-1	47.03	1.13	4	826-849	776	816	24.15	Giordano et al. (2015)
30	Trachybasalt	Bet1-3	47.03	1.64	6	805-850	769	809	23.62	Giordano et al. (2015)
31	Trachybasalt	802-1	47.03	2.31	3	797-818	732	772	25.03	Giordano et al. (2015)
32	Trachyte	Trach_0.0	69.00	0.00	24	951-1929	965	1025	12.79	Bouhifd et al. (2006)
33	Trachyte	Trach_0.57	69.00	0.57	9	879-989	865	925	15.59	Bouhifd et al. (2006)
34	Trachyte	Trach_2.2	69.00	2.19	9	725-802	740	800	16.36	Bouhifd et al. (2006)
35	Trachyte	Trach_5	69.00	4.92	3	621-640	640	700	17.07	Bouhifd et al. (2006)
36	Bas. Andesite	sbadry	54.42	0.01	18	983-1836	1010	-	21.09	Robert et al. (2014)
37	Bas. Andesite	sba-10	54.42	0.50	7	909-961	928	-	22.19	Robert et al. (2014)
38	Bas. Andesite	sba-11	54.42	0.95	6	863-910	886	-	24.14	Robert et al. (2014)
39	Bas. Andesite	sba-04	54.42	2.00	7	805-855	826	-	25.42	Robert et al. (2014)
40	Bas. Andesite	sba-03	54.42	2.92	6	763-816	777	-	27.43	Robert et al. (2014)
41	Bas. Andesite	sba-07	54.42	3.76	6	739-759	740	-	26.23	Robert et al. (2014)
42	Bas. Andesite	fu06dry	49.40	0.01	9	912-994	950	-	23.10	Robert et al. (2014)
43	Bas. Andesite	fu06-07	49.40	1.18	7	845-889	842	-	27.93	Robert et al. (2014)
44	Bas. Andesite	fu06-06	49.40	1.44	7	826-865	819	-	27.53	Robert et al. (2014)
45	Bas. Andesite	fu06-03	49.40	2.29	7	783-811	775	-	28.94	Robert et al. (2014)
46	Bas. Andesite	fu06-04	49.40	2.70	4	757-783	753	-	30.30	Robert et al. (2014)
47	Albite-dry	HAB0	75.30	0.00	14	1004-1141	1096	1156	4.85	Bouhifd et al. (2006)
48	Albite-hydrous	HAB2.2	75.30	1.87	8	701-778	690	750	10.45	Bouhifd et al. (2006)
49	Haplogranite	HPG-8	78.60	0.02	13	1178-1916	1073	-	8.00	Hess et al. (1996)
50	Rhyolite	R_R_Lipari	73.80	0.00	13	1173-1923	873	1016	14.04	pers. comm Giordano

Table 2. Data for modelling temperature dependence of viscosity (η) for 4 melts using Adam-Gibbs equation including: number of measurements of η (*N*) over the temperature range (*ΔT*), and values of Cp_c and Tg_{Onset}. Model values of *A*, *B* and S_c are reported for individual fits and for fitting of the entire data set assuming a common value of *A*. Also reported are calculated values of glass transition temperature (Tg^{12}) and fragility (m). Data are from Giordano et al. (2005) and Bouhifd et al. (2006) (cf. Table 1).

Label	Etn_0	Etn_1.64	Phon_0	Phon_0.5
Composition	Trachybasalt	Trachybasalt	Phonolite	Phonolite
SiO_2	47.03	47.03	65.4	65.4
TiO_2	1.61	1.61	0.66	0.66
Al_2O_3	16.28	16.28	12.72	12.72
FeO(T)	10.88	10.88	0	0
MnO	0.2	0.2	0	0
MgO	5.17	5.17	3.1	3.1
CaO	10.47	10.47	2.8	2.8
Na_2O	3.75	3.75	10.04	10.04
K_2O	1.94	1.94	5.28	5.28
P_2O_5	0.59	0.59	0	0
H_2O	0.02	1.64	0	0.78
Adam Gibbs Model Individual Fits				
N	10	6	20	11
ΔT (K)	985-1818	805-850	889-1816	819-925
Cp_c (J mol^{-1} K^{-1})	21.05	23.62	11.68	13.59
Tg_{Onset} (K)	954	769	915	802
A (Pa s)	-3.78	2.57	-2.02	-6.76
B (kJ mol^{-1})	179.5	60.24	130.9	478.8
S_c (J mol^{-1} K^{-1})	11.76	7.54	10.11	30.49
Tg^{12} (η~ 10^{12} Pa s)	967.5	847.1	923.8	837.1
m	44.0	39.0	30.2	27.1
Adam Gibbs Model with Common A				
A_{AG} (Pa s)		-2.29		
B_{AG} (kJ mol^{-1})	90.3	207.7	145.2	166.0
S_c (J mol^{-1} K^{-1})	6.37	18.57	11.07	14.05
Tg_{AG} (K)	992.0	932.1	1093.0	984.6
m_{AG}	61.5	27.3	24.7	23.6

Table 3. Model deerived from fitting all data to Adam Gibbs equation with a common A_{AG} (-3.51) and independent values of B_{AG} and S_c. Values of Cp_c/S_c, Tg^{12} and m calculated from this model (see text) and from the GRD model for melt viscosity (Giordano et al. 2008).

Label	SM_H	NBO/T_H	Tg_{onset}	Cp_c	B_{AG}	S_c	Cp_c / S_c	Tg^{12}	m	Predicted by GRD (A_{VFT} = -4.55)				
										B_{VFT}	C_{VFT}	Tg^{12}	m	Cp_c / S_c
			(K)	(J/mol K)	(kJ/mol)	(J/mol K)						(K)		
An100_dry	26.11	0.04	1121.6	25.29	164.42	9.37	2.70	1131	57.4	2834	779.5	950.7	91.9	4.55
An10Di90H2	48.12	1.69	827.85	24.23	194.58	15.05	1.61	833	40.5	6013	464.4	827.7	37.7	1.28
An10Di90H3	48.22	1.70	822.45	26.42	223.89	17.54	1.51	823	38.9	6013	462.7	826.1	37.6	1.27
An10Di90H4	49.51	1.79	776.55	28.76	204.72	16.75	1.72	788	42.1	6006	446.0	808.9	36.9	1.23
An42Di58H1	41.57	0.93	883.15	25.02	232.06	16.88	1.48	886	38.5	4726	551.5	837.0	48.5	1.93
An42Di58H3	44.65	1.09	788.4	25.72	315.68	25.59	1.00	795	31.1	4725	507.9	793.4	46.0	1.78
An90Di10H2	34.00	0.33	843.3	25.72	339.45	26.08	0.99	839	30.8	3290	580.3	779.0	64.9	2.92
DK-89	8.18	0.04	975	8.93	162.46	10.57	0.84	991	28.6	12094	289.6	1020.4	23.1	0.40
FR_Dry	18.79	0.16	929.2	16.4	203.19	13.44	1.22	975	34.4	7686	481.5	945.9	33.7	1.04
FR_1.6	22.90	0.28	756.5	19.2	283.28	23.32	0.82	783	28.3	7505	314.4	767.9	28.0	0.69
FR_2.7	25.81	0.39	678.9	16.12	195.13	17.60	0.92	715	29.7	7301	277.4	718.5	27.0	0.63
FR_3.8	28.56	0.48	641.1	14.49	175.47	16.60	0.87	681	29.0	7110	253.4	683.0	26.3	0.59
FR_6.3	34.36	0.71	598.9	14.04	153.52	15.42	0.91	642	29.6	6715	213.4	619.1	25.3	0.53
PS_0	10.10	0.10	806.1	11.16	387.70	31.10	0.36	804	21.1	9775	310.9	901.5	25.3	0.53
PS 0.5	12.44	0.16	697.9	12.18	139.36	12.60	0.97	713	30.5	9703	194.2	780.5	22.0	0.33
PS 1.1	13.63	0.19	666.4	12.92	184.76	17.75	0.73	671	26.8	9618	161.3	742.4	21.1	0.28
PS 2.2	16.58	0.28	633.8	13.68	220.03	22.61	0.60	627	24.9	9374	112.8	679.2	19.8	0.20
PS 3.5	20.17	0.38	583.3	14.28	140.57	15.19	0.94	597	30.1	9141	76.1	628.5	18.8	0.14
Phon-0.0	22.02	0.33	915	11.68	235.07	16.57	0.71	915	26.4	9302	294.0	856.0	25.2	0.52
Phon_0.5(B)	24.13	0.39	802	13.59	221.24	17.26	0.79	826	27.7	9201	166.4	722.3	21.5	0.30
Phon_2.2	27.66	0.51	690	15.67	295.36	27.84	0.56	684	24.2	8859	90.7	626.0	19.4	0.17
Phon_5	33.67	0.74	592	16.06	220.21	23.84	0.67	596	26.0	8244	27.1	525.3	17.5	0.05

NIQ_0	48.90	1.51	916	23.36	145.89	10.27	2.27	916	50.8	4495	653.2	924.8	56.4	2.40
NIQ_0.68	50.03	1.59	850	25.66	185.36	14.07	1.82	850	43.8	4610	550.6	829.1	49.3	1.98
Teph_Dry	38.49	0.86	933	23.54	172.95	12.02	1.96	928	45.9	5910	570.5	927.5	43.0	1.60
Teph_1.5	41.73	1.02	814	27.49	328.75	26.02	1.06	815	31.9	5927	409.7	767.8	35.5	1.14
Etn_0	27.14	0.47	954.2	21.05	160.49	10.82	1.95	956	45.7	5494	602.6	934.5	46.6	1.82
801-1	28.78	0.53	836.2	21.66	407.62	31.54	0.69	833	26.2	5570	503.6	840.1	41.3	1.50
800-1	30.04	0.57	776.15	24.15	434.95	35.29	0.68	795	26.1	5568	470.4	806.8	39.7	1.40
Bet1-3	31.31	0.63	769.2	23.62	271.33	22.28	1.06	785	32.0	5552	448.5	783.9	38.7	1.34
802-1	32.92	0.69	732.15	25.03	351.80	30.56	0.82	742	28.2	5521	429.1	762.6	37.8	1.29
Trach_0.0	22.36	0.38	965	12.79	218.81	14.62	0.87	965	29.1	9076	376.6	925.0	27.9	0.69
Trach_0.57	23.85	0.43	865	15.59	240.33	17.55	0.89	883	29.3	9047	272.9	819.6	24.8	0.50
Trach_2.2	27.90	0.56	740	16.36	328.87	28.93	0.57	733	24.3	8725	178.0	705.3	22.1	0.34
Trach_5	34.07	0.80	640	17.07	227.75	23.38	0.73	628	26.8	8175	114.8	608.7	20.4	0.23
sbadry	29.32	0.40	1010	21.09	199.03	13.01	1.62	987	40.7	6162	592.3	964.7	42.9	1.59
sba-10	30.51	0.44	928	22.19	202.12	14.47	1.53	900	39.3	6204	503.7	878.6	38.8	1.34
sba-11	31.59	0.48	886	24.14	285.72	21.42	1.13	860	33.0	6184	466.1	839.8	37.2	1.25
sba-04	34.00	0.57	826	25.42	295.71	23.61	1.08	807	32.2	6090	420.0	788.0	35.4	1.14
sba-03	36.01	0.65	777	27.43	330.32	27.73	0.99	768	30.9	5997	397.1	759.4	34.7	1.10
sba-07	37.78	0.73	740	26.23	174.20	15.36	1.71	731	42.0	5913	382.0	739.2	34.2	1.07
fu06dry	25.83	0.40	950	23.1	171.23	11.84	1.95	933	45.8	5270	612.5	930.9	48.4	1.92
fu06-07	28.80	0.51	842	27.93	223.81	17.24	1.62	837	40.6	5374	477.6	802.4	40.9	1.47
fu06-06	29.43	0.53	819	27.53	193.08	15.17	1.81	821	43.7	5372	466.3	790.9	40.3	1.44
fu06-03	31.46	0.62	775	28.94	216.20	18.07	1.60	771	40.3	5353	441.0	764.5	39.1	1.36
fu06-04	32.41	0.66	753	30.3	261.44	22.82	1.33	739	36.1	5340	432.6	755.3	38.7	1.34
HAB0	12.93	0.11	1096	4.85	183.75	11.68	0.42	1014	22.0	10995	207.2	871.6	21.7	0.31
HAB2.2	18.41	0.26	690	10.45	278.09	25.19	0.41	712	21.9	10438	7.9	638.6	16.8	0.01
HPG-8	7.67	0.00	1073	8.0	236.38	13.72	0.58	1111	24.6	12744	325.1	1095.1	23.5	0.42
R_R_Lipari	8.55	0.003	873.15	14.04	445.68	27.79	0.51	1034	23.3	11492	311.7	1006.2	24.0	0.45

Table A.1. Chemical compositions as wt. % oxides for experimental melts used in this study; oxides not measured indicated as (-).

Label	Composition	SiO_2	TiO_2	Al_2O_3	FeO(T)	MnO	MgO	CaO	Na_2O	K_2O	P_2O_5	H_2O	Source
An100	Anorthite	42.90	-	35.10	0.07	-	0.08	20.70	0.18	0.02	-	0.00	Solvang et al. (2005)
An10Di90H2	An-Di	55.60	-	4.47	0.01	-	14.60	24.70	0.09	0.00	-	1.69	This Work
An10Di90H3	An-Di	55.60	-	4.47	0.01	-	14.60	24.70	0.09	0.00	-	1.75	This Work
An10Di90H4	An-Di	55.60	-	4.47	0.01	-	14.60	24.70	0.09	0.00	-	2.58	This Work
An42Di58H1	An-Di	49.60	-	17.20	0.08	-	9.75	22.70	0.12	0.05	-	1.05	This Work
An42Di58H3	An-Di	49.60	-	17.20	0.08	-	9.75	22.70	0.12	0.05	-	2.70	This Work
An90Di10H2	An-Di	44.60	-	32.40	0.02	-	1.43	20.50	0.04	0.01	-	2.56	This Work
DK-89	Dacite	80.25	0.14	9.93	0.81	0.00	0.31	0.98	4.15	3.43	0.00	0.00	Bouhifd et al. (2006)
FR_Dry	Latite	56.63	0.82	18.00	6.70	0.17	2.41	5.60	4.61	4.56	0.46	0.02	Di Genova et al. (2014)
FR_1.6	Latite	55.74	0.81	17.72	6.59	0.17	2.37	5.51	4.53	4.49	0.46	1.59	Di Genova et al. (2014)
FR_2.7	Latite	55.12	0.80	17.52	6.52	0.17	2.34	5.45	4.48	4.44	0.45	2.69	Di Genova et al. (2014)
FR_3.8	Latite	54.51	0.79	17.33	6.45	0.17	2.32	5.39	4.43	4.39	0.45	3.76	Di Genova et al. (2014)
FR 6.3	Latite	53.06	0.77	16.87	6.27	0.16	2.26	5.25	4.32	4.28	0.43	6.32	Di Genova et al. (2014)
PS_0	Pantellerite	70.35	0.49	9.15	9.56	0.39	0.08	0.58	5.87	4.10	0.03	0.02	Di Genova et al. (2014)
PS 0.5	Pantellerite	69.89	0.49	9.09	9.50	0.38	0.08	0.57	5.83	4.07	0.04	0.72	Di Genova et al. (2014)
PS 1.1	Pantellerite	69.56	0.51	9.08	9.39	0.38	0.08	0.59	5.76	4.02	0.02	1.16	Di Genova et al. (2014)
PS 2.2	Pantellerite	68.67	0.49	9.00	9.28	0.36	0.06	0.60	5.82	4.02	0.04	2.11	Di Genova et al. (2014)
PS 3.5	Pantellerite	68.43	0.49	8.94	9.06	0.39	0.08	0.57	5.17	4.02	0.03	3.55	Di Genova et al. (2014)
Phon-0.0	Phonolite	65.40	0.66	12.72	0.00	0.00	3.10	2.80	10.04	5.28	0.00	0.00	Bouhifd et al. (2006)
Phon_0.5(B)	Phonolite	65.40	0.66	12.72	0.00	0.00	3.10	2.80	10.04	5.28	0.00	0.78	Bouhifd et al. (2006)
Phon_2.2	Phonolite	65.40	0.66	12.72	0.00	0.00	3.10	2.80	10.04	5.28	0.00	2.15	Bouhifd et al. (2006)
Phon_5	Phonolite	65.40	0.66	12.72	0.00	0.00	3.10	2.80	10.04	5.28	0.00	4.72	Bouhifd et al. (2006)
NIQ_0	Tephrite	43.57	2.97	10.18	0.00	0.00	9.17	26.07	7.59	0.96	0.00	0.00	Bouhifd et al. (2013)
NIQ_0.68	Tephrite	43.57	2.97	10.18	0.00	0.00	9.17	26.07	7.59	0.96	0.00	0.68	Bouhifd et al. (2013)
Teph_Dry	Tephrite	50.56	2.35	14.03	0.00	0.00	8.79	15.00	7.04	3.01	0.00	0.00	Bouhifd et al. (2013)
Teph_1.5	Tephrite	50.56	2.35	14.03	0.00	0.00	8.79	15.00	7.04	3.01	0.00	1.60	Bouhifd et al. (2013)

Etn_0	Trachybasalt	47.03	1.61	16.28	10.88	0.20	5.17	10.47	3.75	1.94	0.59	0.02	Giordano et al. (2005)
801-1	Trachybasalt	47.03	1.61	16.28	10.88	0.20	5.17	10.47	3.75	1.94	0.59	0.64	Giordano et al. (2005)
800-1	Trachybasalt	47.03	1.61	16.28	10.88	0.20	5.17	10.47	3.75	1.94	0.59	1.13	Giordano et al. (2005)
Bet1-3	Trachybasalt	47.03	1.61	16.28	10.88	0.20	5.17	10.47	3.75	1.94	0.59	1.64	Giordano et al. (2005)
802-1	Trachybasalt	47.03	1.61	16.28	10.88	0.20	5.17	10.47	3.75	1.94	0.59	2.31	Giordano et al. (2005)
Trach_0.0	Trachyte	69.00	0.40	10.54	0.00	0.00	4.66	6.15	6.95	2.30	0.00	0.00	Bouhifd et al. (2006)
Trach_0.57	Trachyte	69.00	0.40	10.54	0.00	0.00	4.66	6.15	6.95	2.30	0.00	0.57	Bouhifd et al. (2006)
Trach_2.2	Trachyte	69.00	0.40	10.54	0.00	0.00	4.66	6.15	6.95	2.30	0.00	2.19	Bouhifd et al. (2006)
Trach_5	Trachyte	69.00	0.40	10.54	0.00	0.00	4.66	6.15	6.95	2.30	0.00	4.92	Bouhifd et al. (2006)
sbadry	Bas. Andesite	54.42	1.37	20.49	0.00	0.00	8.40	10.39	3.76	1.06	0.00	0.01	Robert et al. (2014)
sba-10	Bas. Andesite	54.42	1.37	20.49	0.00	0.00	8.40	10.39	3.76	1.06	0.00	0.50	Robert et al. (2014)
sba-11	Bas. Andesite	54.42	1.37	20.49	0.00	0.00	8.40	10.39	3.76	1.06	0.00	0.95	Robert et al. (2014)
sba-04	Bas. Andesite	54.42	1.37	20.49	0.00	0.00	8.40	10.39	3.76	1.06	0.00	2.00	Robert et al. (2014)
sba-03	Bas. Andesite	54.42	1.37	20.49	0.00	0.00	8.40	10.39	3.76	1.06	0.00	2.92	Robert et al. (2014)
sba-07	Bas. Andesite	54.42	1.37	20.49	0.00	0.00	8.40	10.39	3.76	1.06	0.00	3.76	Robert et al. (2014)
fu06dry	Bas. Andesite	49.40	0.96	17.57	10.56	0.00	7.46	8.97	3.10	0.60	0.16	0.01	Robert et al. (2014)
fu06-07	Bas. Andesite	49.40	0.96	17.57	10.56	0.00	7.46	8.97	3.10	0.60	0.16	1.18	Robert et al. (2014)
fu06-06	Bas. Andesite	49.40	0.96	17.57	10.56	0.00	7.46	8.97	3.10	0.60	0.16	1.44	Robert et al. (2014)
fu06-03	Bas. Andesite	49.40	0.96	17.57	10.56	0.00	7.46	8.97	3.10	0.60	0.16	2.29	Robert et al. (2014)
fu06-04	Bas. Andesite	49.40	0.96	17.57	10.56	0.00	7.46	8.97	3.10	0.60	0.16	2.70	Robert et al. (2014)
HAB0	Albite-dry	75.30	0.00	12.07	0.00	0.00	0.00	0.00	12.62	0.00	0.00	0.00	Bouhifd et al. (2006)
HAB2.2	Albite-hydrous	75.30	0.00	12.07	0.00	0.00	0.00	0.00	12.62	0.00	0.00	1.87	Bouhifd et al. (2006)
HPG-8	Haplogranite	78.60	0.00	12.50	0.00	0.00	0.00	0.00	4.60	4.20	0.00	0.02	Hess et al. (1996)
R_R_Lipari	Rhyolite	73.80	0.08	12.95	1.57	0.06	0.04	0.75	3.72	5.05	0.01	0.00	pers. comm Giordano

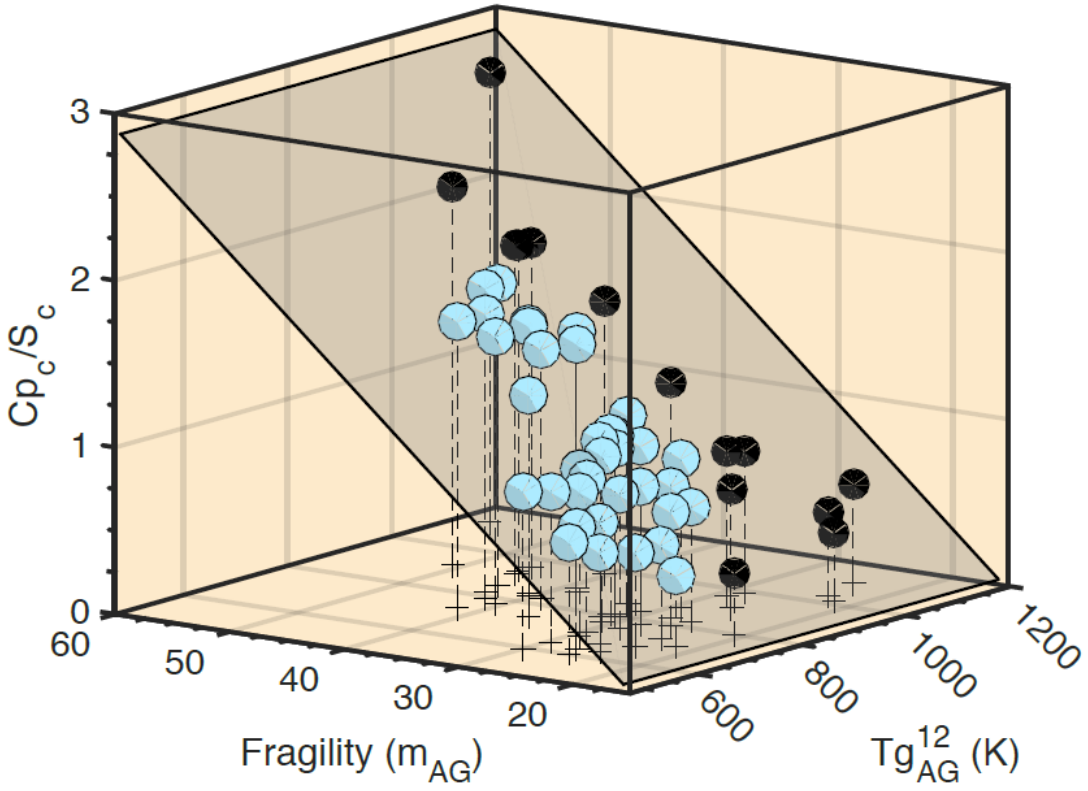

Graphical abstract